Strain Engineering of the Electronic States of Silicon-Based Quantum Emitters

Andrea Ristori, Mario Khoury, Marco Salvalaglio, Angelos Filippatos, Michele Amato, Tobias Herzig, Jan Meijer, Sebastien Pezzagna, Drisse Hannani, Monica Bollani, Chiara Barri, Carmen M. Ruiz, Nicoletta Granchi, Francesca Intonti, Marco Abbarchi,* and Francesco Biccari

Light-emitting complex defects in silicon have been considered a potential platform for quantum technologies based on spin and photon degrees of freedom working at telecom wavelengths. Their integration in complex devices is still in its infancy and has been mostly focused on light extraction and guiding. Here the control of the electronic states of carbon-related impurities (G-centers) is addressed via strain engineering. By embedding them in patches of silicon on insulator and topping them with SiN, symmetry breaking along [001] and [110] directions is demonstrated, resulting in a controlled splitting of the zero phonon line (ZPL), as accounted for by the piezospectroscopic theoretical framework. The splitting can be as large as 18 meV, and it is finely tuned by selecting patch size or by moving in different positions on the patch. Some of the split, strained ZPLs are almost fully polarized, and their overall intensity is enhanced up to 7 times with respect to the flat areas, whereas their recombination dynamics is slightly affected accounting for the lack of Purcell effect. This technique can be extended to other impurities and Si-based devices such as suspended bridges, photonic crystal microcavities, Mie resonators, and integrated photonic circuits.

1. Introduction

Strain engineering is a key and versatile scheme to efficiently design and improve the properties of nanostructures and nanodevices. This technique was used with great success in various fields to modify fundamental materials properties[1] - such as electronic band gap, band splitting, effective mass, and scattering processes - leading to enhanced device performances. Successful applications of strain-engineered materials include CMOS components,[2,3] graphene and 2D materials,[4,5] III-nitride membranes for LEDs,[6,7] sensing platforms,[8,9] III-V and IV-IV epitaxial-grown nanostructures.[10–12] Strain control is particularly relevant for Silicon (Si)-based light sources, such as color-centers, which require individual emitters' tunability for future scaling up. The properties of each emitting center

A. Ristori, N. Granchi, F. Intonti, F. Biccari
European Laboratory for Non-Linear Spectroscopy (LENS)
Via N. Carrara 1, Sesto Fiorentino (FI) I-50019, Italy

A. Ristori, N. Granchi, F. Intonti, F. Biccari
Department of Physics and Astronomy
University of Florence
Via G. Sansone 1, Sesto Fiorentino (FI) I-50019, Italy

M. Khoury, D. Hannani, C. M. Ruiz, M. Abbarchi
Aix Marseille Univ, CNRS
Université de Toulon
IM2NP, UMR 7334, Marseille F-13397, France
E-mail: marco.abbarchi@im2np.fr

M. Salvalaglio
Institute of Scientific Computing
TU Dresden, 01062 Dresden, Germany

M. Salvalaglio, A. Filippatos
Dresden Center for Intelligent Materials (DCIM)
TU Dresden, 01062 Dresden, Germany

A. Filippatos
Department of Mechanical Engineering & Aeronautics
University of Patras
Patras GR-26504, Greece

M. Amato
Laboratoire de Physique des Solides
Université Paris-Saclay
CNRS, Orsay, Paris 91405, France

T. Herzig, J. Meijer, S. Pezzagna
Division of Applied Quantum Systems, Felix-Bloch Institute for Solid-State Physics
University Leipzig
Linnéstrasse 5, 04103 Leipzig, Germany

M. Bollani
Istituto di Fotonica e Nanotecnologie-Consiglio Nazionale delle Ricerche
Laboratory for Nanostructure Epitaxy and Spintronics on Silicon
Via Anzani 42, Como 22100, Italy

can be independently changed by applying a mechanical deformation in its local environment. As a matter of fact, Si light emitters based on complex impurities[13,14] are currently scrutinized for their applicability as photon and spin quantum-bits.[15] Their appeal is manyfold: 1) they are nominally identical and in ensemble emission, they have a sharp zero phonon line (ZPL) featuring a broadening of about 10 μeV in conventional Si and less than 1 μeV (about 10^{-3} nm) in spin-less, isotopically purified ^{28}Si[14]; 2) their ZPL lies below the Si band-gap, in the near-infrared range (1.15 to 1.45 μm), covering the telecommunication O, E, and S bands[16,17]; 3) their recombination lifetime can be as short as a few ns[18–20]; 4) they are stable in temperature and time (no bleaching nor blinking)[19,21] and can be detected up 120 K[22]; 5) they have well-defined polarization axes.[17,19,21]

Beyond these intrinsic properties that are unmatched by their counterparts in other materials, the possibility to exploit them in quantum technologies is highly entrancing, provided the advantages that this solid-state platform offers. Silicon technology steps on all the nano-fabrication methods developed in the last 50 years for electronic devices and it is, by far, more advanced than the technology applied to any other material: fabrication of electronic components can be provided in an industrial production chain with high material purity (99.9999999%, *nine nines*), large wafers up to 17 inches, silicon on insulator (SOI) wafers up to 12 inches, *p* and *n* doping, top-down lithography with nanometric resolution (e.g. based on deep-UV and plasma etching), availability of isotopically purified ^{28}Si wafers.[23–28]

The renewed interest in this class of Si-based emitters in the context of quantum technologies resulted in several breakthroughs over the last few years with the demonstration of 1) single-photon emission from a large zoology of well-known (e.g. G-, W-, T-centers) and unknown defects[17,19–21,29,30]; 2) photon coalescence[31]; 3) spin control[32–34]; 4) integration in photonic devices, such as Mie resonators,[22,34,35] integrated photonic circuits,[30,31,36] ring resonators,[37] and photonic crystals[38,39] providing Purcell effect; 5) position control of the emitters with localized ion implant[40]; 6) coherent population trapping and Autler-Townes splitting.[41]

Most of these works focused on defect creation, enhancement of light emission, extraction, and guiding, in order to better detect and manipulate these single photon sources. A further step to control their properties requires a precise tuning of the photoluminescence frequency and its polarization (e.g. for setting the coupling of the ZPL with a photonic resonance).

In this paper, we show that a large and tunable splitting of the ZPL of G-centers can be simply obtained through strain engineering by etching square patches in a [001]-oriented SOI wafer followed by deposition of SiN via plasma-enhanced chemical vapor deposition (PE-CVD). Compressive and tensile strain is obtained by adjusting the plasma frequency during SiN deposition,
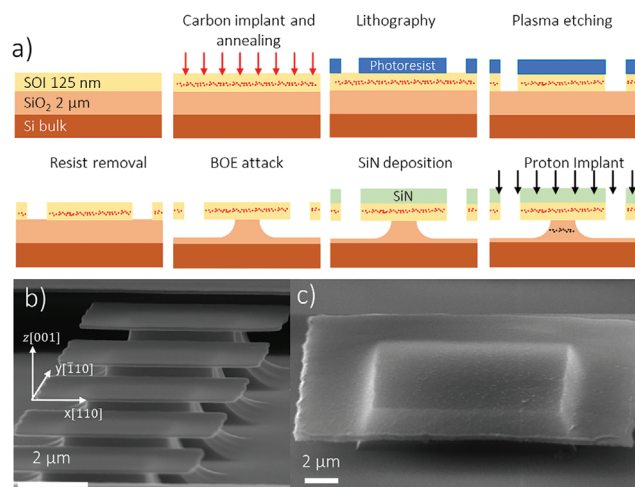
C. Barri
L-NESS, Dipartimento di Fisica
Politecnico di Milano
Como 20133, Italy
M. Abbarchi
Solnil
95 Rue de la République, Marseille 13002, France

Figure 1. *Sample fabrication.* a) A 125 nm thick SOI sample is implanted with carbon ions and recrystallized by annealing at high temperature (1000 °C for 10 seconds in N_2 atmosphere). By optical lithography, square patches with variable side lengths are defined. The buried oxide underneath the SOI patches was partially removed via chemical etching using a buried-oxide etcher (BOE). SiN is deposited via plasma-enhanced chemical vapor deposition (PE-CVD). G-center activation is performed via proton implant. Details of the sample fabrication are provided in the dedicated section and in Table 1. b) Scanning electron micrograph (SEM) of SOI patches before SiN deposition. c) SEM of a strained SOI patch with SiN atop.

as confirmed by Raman spectroscopy. Symmetry breaking of the silicon unit cell along the vertical [001] direction is obtained at the center of the square patches, whose size sets the magnitude of the strain and thus the corresponding ZPL splitting in two main lines. Moving from the center of a patch towards the suspended (leaning) part, the symmetry breaking occurs also along the ⟨110⟩ directions leading to a splitting of the ZPL in four lines. Finite element methods calculations of the strain coupled to the *piezospectroscopic* theory[42] confirms the overall picture observed in photoluminescence measurements. Partial or total polarization of the split ZPLs accounts for the alignment of the emitting dipoles along specific crystallographic directions. Embedding the emitters in these structures entails an intensity enhancement of their photoluminescence up to a factor of 7 with respect to the flat counterpart, which is ascribed to a larger extraction of light, as confirmed by time-resolved experiments and finite element simulations.

2. Results

2.1. Sample Fabrication

A detailed description of sample fabrication is provided in the dedicated section at the end of the paper (Section 4.1). Here we refer to **Figure 1** where the main fabrication steps and some real examples are shown: a 125 nm thick SOI is implanted with C ions and recrystallized by annealing. The underlying SiO_2 is partially removed with a diluted HF acid. The samples are then topped with SiN and etched by optical lithography in square patches having different side lengths *L*. Finally, proton implant is used to activate the emitting G-centers.

**ADVANCED
SCIENCE NEWS**

www.advancedsciencenews.com

**ADVANCED
OPTICAL
MATERIALS**

www.advopticalmat.de

Table 1. List of samples and fabrication parameters: carbon implant energy and corresponding depth, and carbon dose; PE-CVD deposition conditions for SiN including high-frequency plasma time fraction (HF%), high-frequency and low-frequency plasma power (HF, LF) corresponding type of strain (compressive or tensile, C or T), SiN thickness as measured by ellipsometry; proton implant energy and corresponding depth, and proton dose.

Sample	C ions implant		PE-CVD				Proton implant	
	Energy (Depth) keV (nm)	Dose 10^{14} cm^{-2}	HF Plasma time %	Plasma Power HF, LF (W)	Strain C, T	SiN nm	Energy (Depth) keV (nm)	Dose 10^{14} cm^{-2}
A	6 (25)	5.5	0	0, 100	C	108	90 (830)	1
B	6 (25)	5.5	100	300, 0	T	102	90 (830)	1
C	30 (100)	6.5	70	20, 80	T	100	90 (830)	1

In this work, we study three samples with etched patches. The details of their fabrication conditions are provided in **Table 1**.

2.2. Finite Element Method Simulations of Strained Patches

We provide a theoretical description of the elastic field in the strained patches via finite element method (FEM) calculations. Details of the method are provided in Section 4.1. This analysis assesses the SOI deformation due to the action of the SiN stressor, thus allowing for the detailed explanation of the photoluminescence results, and independently complements the Raman spectroscopy results reported in the Supplemental Information. Without loss of generality, we focus first on a system where the length of the side of the membrane (L) is 10 µm (**Figure 2**). Moreover, we consider a SiN layer featuring a compressive in-plane deformation resulting in strain-field components $\varepsilon_{\tilde{x}\tilde{x}}$, $\varepsilon_{\tilde{y}\tilde{y}}$ and $\varepsilon_{\tilde{z}\tilde{z}} \equiv \varepsilon_{zz}$ with $\tilde{x} = [110]$, $\tilde{y} = [1\bar{1}0]$, and $z = \tilde{z} = [001]$ conveniently chosen to discuss effects on the Si crystal unit cell (while the canonical frame of reference is considered in the following when referring to x, y, z directions).

For a flat film configuration, a tetragonal distortion of the stressor would occur with a linear out-of-plane displacement, no in-plane deformation, and no strain partitioning[44] (not shown), as actually measured by Raman spectroscopy for L = 50 µm (thus approaching the flat film case, see the Supplemental Information provided at the end of this document).

For smaller membranes, additional free surfaces introduce extra elastic relaxation with strain partitioning among the stressor and the substrate, i.e. the Si layer. In particular, the SiN stressor induces an in-plane strain of the opposite sign in the Si layer and an out-of-plane strain with the same sign of the stressor in-plane strain, as observed in general for heterostructures exhibiting lateral free surfaces[45,46] (Figure 2b).

At the center of the structure ("center" in Figure 2a), owing to the small relative thickness of the SiN/Si bilayer compared to their lateral size, a film-like configuration is obtained, and all the strain components vary negligibly along z, top panel) and $\varepsilon_{\tilde{x}\tilde{x}} = \varepsilon_{\tilde{y}\tilde{y}}$ (Figure 2c). As such, an isotropic in-plane deformation is achieved: in the plane of the patch the symmetry of the Si unit cell is preserved, whereas it is broken along z under the action of ε_{zz} that differs from the in-plane value.

When moving towards the edge of the SiO$_2$ pedestal ("boundary", Figure 2b-d), the crystal unit cells are deformed asymmetrically along $\tilde{x}$ and $\tilde{y}$, owing to different actions of free surfaces with normal along these directions (Figure 2b)). Similar
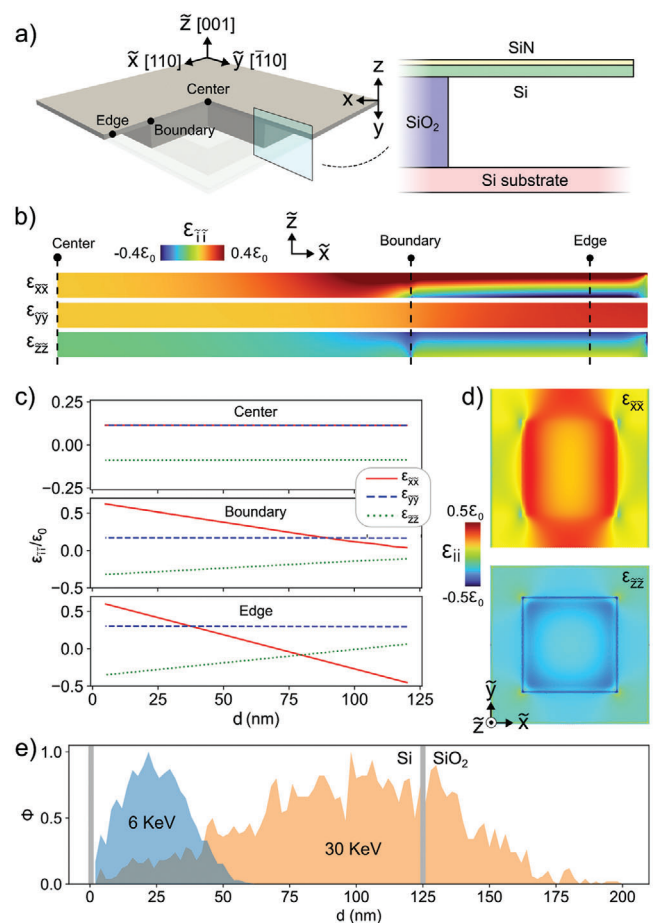

Figure 2. *Simulation of the elastic field.* a) Geometry in a perspective view (left) and 2D cross section highlighting the different materials (right). Three representative points are marked: "*center*", "*boundary*" between the leaning and suspended SiN/Si bilayer, and "*edge*" in the leaning part of the patch. b) Strain field in a ($\bar{1}$10) cross-section of the Si layer. Thickness is magnified (× 2) for visualization purposes. c) Strain field components in the SOI layer as a function of the depth (d corresponds to the z direction [00$\bar{1}$]) from the SiN/SOI interface (d = 0) at three (x, y) points (center, boundary, and edge, as illustrated in panel a). d) Strain field component in the (001) plane at d = 62.5 nm. e) Normalized distributions of implanted carbon ions (Φ) as a function of the depth in the SOI layer and in the SiO$_2$ BOX for two beam energies, namely 6 keV and 30 keV, obtained by SRIM software.[43]

**ADVANCED
SCIENCE NEWS**

www.advancedsciencenews.com

**ADVANCED
OPTICAL
MATERIALS**

www.advopticalmat.de

asymmetric behavior is obtained in the free-standing part of the SiN/SOI bilayer. Here, significant variations of the strain values occur along the vertical direction (Figure 2c), central and bottom panels).

The deformation close to the edges of the membrane can be interpreted in terms of the relaxation induced by a stressor on a suspended substrate with lateral free surfaces, known to lead to a bending of the bilayer.[47] A bending downwards is expected for the relaxation of an initially flat bilayer with a compressive strain of the upper layer.

Thus, both in-plane and out-of-plane symmetry-breaking is achieved when moving far from the center. This generally holds true over the whole square area of the membrane featuring additional relaxed region at the corners owing to the proximity of free surfaces with normal along both $\tilde{x}$ and $\tilde{y}$; see $\varepsilon_{\tilde{x}\tilde{x}}$ and $\varepsilon_{\tilde{z}\tilde{z}}$ in the (001) plane at a depth of 62.5 nm in the Si layer in Figure 2d) ($\varepsilon_{\tilde{y}\tilde{y}}$ would correspond to $\varepsilon_{\tilde{x}\tilde{x}}$ rotated by 90°). Therefore, we can conclude that properties depending on the symmetry breaking along the [001] crystallographic direction (i.e. the z direction) are then expected to emerge everywhere. Instead, properties depending on the symmetry breaking along the ⟨110⟩ directions, are expected to emerge close to and at the suspended part of the patches.

Note that the G-centers are placed at different depths d along the vertical z-axis according to the implant energy, with a relatively broad distribution owing to the implant straggling (Figure 2e). At the center of the patch, all the emitters experience the same strain field, irrespective of their implant depth, offering an ideal scenario for strain engineering of electronic states. Moreover, for the sizes considered in this investigation, the strain at the center of the patches is found to scale as $1/L^2$, so it can be well controlled with the lateral side. This information is also supported by finite element simulation of the strain field as a function of the patch side (not shown). However, emitters placed far from the center (close to the edge of the pedestal and in the suspended part) and at different depths would experience different strains. Proper weighting should then be considered to account for the effect on the electronic states.

The information gathered with these simulations is used as input for the *piezospectroscopic* model used to evaluate the splitting of the ZPLs of the G-centers in membranes having different lateral sizes L. The details of the *piezospectroscopic* model are provided in Section 4.1, while the results are discussed in the following section.

2.3. Photoluminescence Spectroscopy of Strained G-Centers

We now address the effect of strain on the G-center ZPL by studying their emission from SOI patches having different L and topped with SiN in different conditions. First, we study the emission from the center of patches (uniaxial symmetry breaking) and later the case of emitters far from the center (biaxial symmetry breaking). The simple case of flat SOI topped with SiN (not yet etched in small patches) is analyzed in detail in the Supplementary Information provided at the end of this document for samples A, B, and C, and compared to the unstrained case.

Symmetry breaking along [001] direction. Microphotoluminescence experiments at the center of the patch

showcase the typical behavior of G-centers under applied uniaxial stress[49] (**Figure 3**a). At this central point, as assessed by calculations illustrated in Section 2.2, the in-plane strain is isotropic (i.e. $\epsilon_{xx} = \epsilon_{yy}$ or, equivalently $\varepsilon_{\tilde{x}\tilde{x}} = \varepsilon_{\tilde{y}\tilde{y}}$), and the symmetry breaking of the Si cubic cell occurs only in the vertical direction [001] under the action of ϵ_{zz} that differs from the in-plane strain. According to Ref. [42], and Equation 4, a double peak appears in the spectrum with two lines having similar brightness and an energy separation $\Delta E_{HE} + \Delta E_{LE}$ that increases for smaller patch sizes. The splittings in energy between the two new lines as a function of $1/L^2$ (with L patch side) are approximately linear for all the samples (Figure 3c) but with larger slopes for high-energy (HE) ZPLs and smaller slopes for low energy (LE) ZPLs. Thus, the largest splitting is observed for the smallest patches and can be as large as 18 meV.

Time-resolved spectroscopy on both HE and LE ZPLs shows only small deviations of the recombination lifetime with respect to the unstrained case (Figure 3b) that is in between 6 and 4 ns. These values are similar to those recently reported for individual G-centers in isotopically purified ^{28}SOI[20] and for ensemble in 220 nm thick SOI.[18] Thus, the strain magnitude attained in these conditions does not modify the recombination dynamics, as also confirmed by the broadening of the HE and LE split lines (FWHM about 1.2 meV) which is not far from the unstrained case.

All this phenomenology is representative of all the investigated samples, irrespective of the nature and magnitude of the applied strain.

The energy shifts calculated at the patches center through the *piezospectroscopic* theory (described at the end of this paper in Section 4.1), using as inputs the strain field obtained by FEM calculations (see Section 2.2), confirm the almost linear dependence of ΔE with $1/L^2$ (**Figure 4**): HE and LE ZPLs shift with different slopes (larger for HE and smaller for LE) as a function of $1/L^2$ as also measured on the patches and unlike previous reports on bulk samples.[49,50]

From a quantitative point of view, the values of the strain field in the structure depend on the eigenstrain ϵ_0 (see also Section 4.1), namely on the magnitude of the strain induced by the SiN layer. A reasonable agreement between theory and experiments can be found for $\epsilon_0 = 1\%$ for the LE split ZPLs, which is consistent with the nominal strain expected by the fabrication procedure, whereas the measured HE slope is larger than the prediction. Several factors can lead to discrepancies between the *piezospectroscopic* theory and the measured splittings: the model holds for bulk crystals and does not account for the complexity of the strain field in ultra-thin patches; measuring the photoluminescence at cryogenic temperature can further change the overall strain distribution with respect to the FDTD model reported here owing to the different thermal expansion coefficients of the SiN stressor, SOI patch, and underlying BOX pedestal. As such, a quantitative agreement between theory and experiments goes beyond the aim of this work.

Symmetry breaking along [001] and [110] direction. Moving from the center of the patch towards its side the Si unit cell is deformed differently along in-plane directions ⟨110⟩ (i.e. $\varepsilon_{\tilde{x}\tilde{x}} \neq \varepsilon_{\tilde{y}\tilde{y}}$) with still $\varepsilon_{\tilde{z}\tilde{z}} \neq 0$ (Figure 2). Moreover, depending on the position on the membrane and on the depth of the emitters (Table 1), the overall strain field applied to the G-centers at different depths can
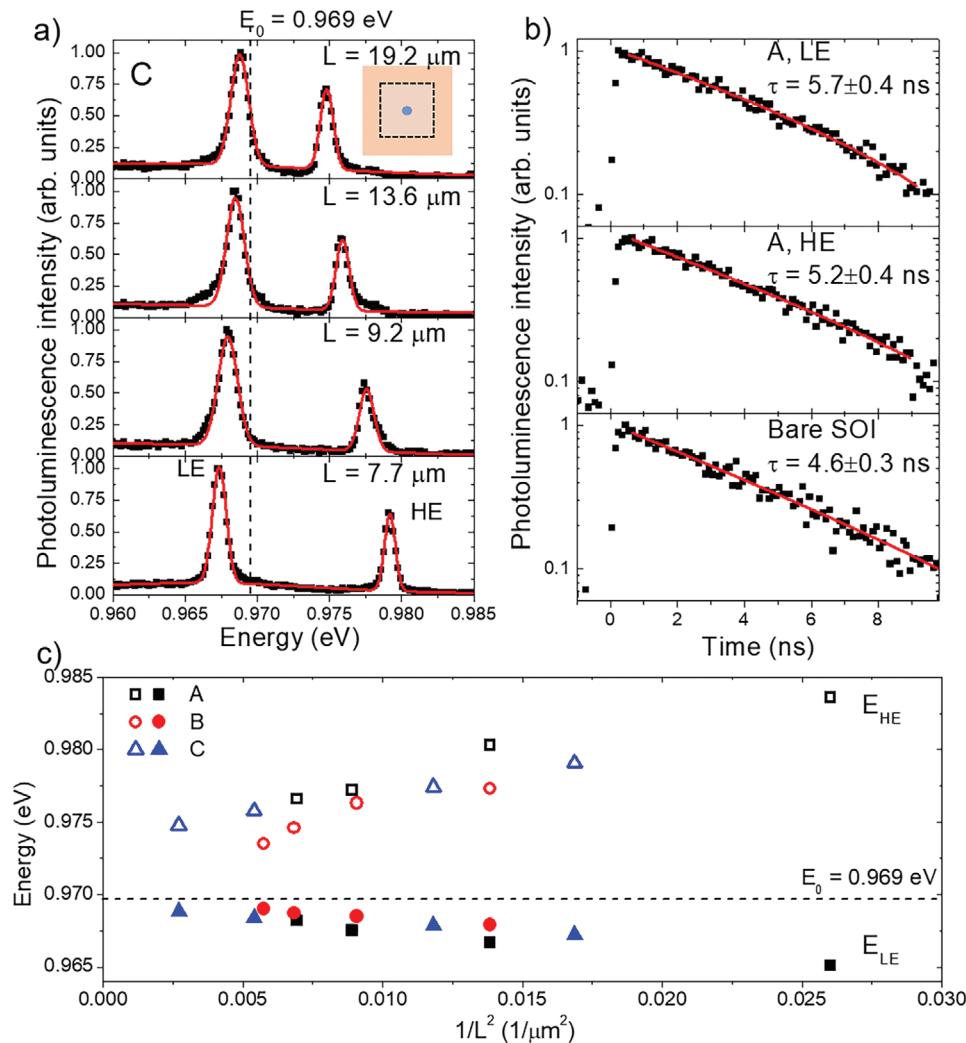
**ADVANCED
SCIENCE NEWS**

www.advancedsciencenews.com

**ADVANCED
OPTICAL
MATERIALS**

www.advopticalmat.de

Figure 3. *Symmetry breaking along [001] direction.* a) Photoluminescence spectra collected at the center of the membrane for different square sides for sample C. The vertical dotted line highlights the energy of the ZPL emission in unstrained samples. The experimental data are represented as square dots whereas the red lines are Gaussian fits. The inset shows the scheme of the membrane highlighting the position of the excitation/collection spot. b) Time-resolved photoluminescence of the ZPL for unstrained SOI, high-energy and low-energy (respectively HE and LE) split components from sample A. The experimental data are represented as square dots whereas the red line is a mono-exponential decay fit. c) Energy of HE and LE ZPL peaks for samples A, B, and C as a function of $1/L^2$. The horizontal dotted line highlights the energy of the ZPL emission in unstrained samples.

be very different (e.g. $\varepsilon_{\bar{x}\bar{x}}$ in the suspended part, at 25 and 100 nm, the strain can change its sign, Figure 2b).

This complex strain field across the patches is reflected in the micro-photoluminescence spectra, as shown in detail for sample B, with G-centers implanted at a depth of about 25 nm from the surface in **Figure 5**. In the inner part (not-leaning, between the vertical dashed lines in Figure 5a), close to the center, the overall picture still resembles the properties of the central part (splitting in two lines of the ZPL). This points to a dominant role of symmetry breaking along the [001] direction with respect to other ones. When moving from the patch center, the two ZPLs undergo a spectral shift to higher energy under the action of the increasing strain. Moreover, owing to i) the onset of symmetry breaking in other directions, ii) the changes of the strain field across the SOI thickness, and iii) the straggling of the ion implant (Figure 2e), HE and LE ZPLs undergo a spectral

broadening when far from the center (up to about 1.8 meV). A clear splitting in four components, that is compatible with symmetry breaking along the [110] direction in addition to that along the [001], is obtained in the suspended part close to the edge of the membrane (see also Figure 5b). A similar picture is found at the angle of the patches, in their suspended parts, where the ZPL is composite and splits into four main components (not shown).

As in the previous case, this symmetry-breaking picture is supported by the *piezospectroscopic* model. Moving from the center towards the patch side, the strain field is not only composed of diagonal components, and the full *piezospectroscopic* Equation 2 has to be considered. By inserting in this equation the simulated strain field and considering the four coefficients estimated in Ref. [48], one obtains different energy shifts (e.g. for a patch with $L = 14$ μm with C implant at a depth of 25 nm, **Figure 6**): moving towards

**ADVANCED
SCIENCE NEWS**

www.advancedsciencenews.com

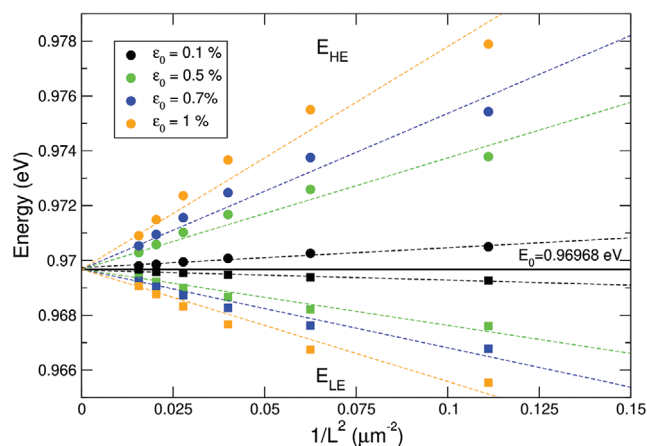**ADVANCED
OPTICAL
MATERIALS**

www.advopticalmat.de

Figure 4. *Theoretical energy shifts for [100] symmetry breaking.* Calculated E_{HE} and E_{LE} energy components at the central point ($x = 0$ and $y = 0$) for different values of the eigenstrain, ϵ_0 and at a depth of 25 nm, as a function of $1/L^2$, with L the side length of the membranes. The energy of the unstrained ZPL is highlighted. The data are derived by inserting in Equation 4 the strain field simulated with FEM and the B_{kl} coefficients from Ref. [48]. The dependence with $1/L^2$ was obtained by calculating E_{HE} and E_{LE} at the central point for $L = 6$ to 16 μm and then fitted for larger values. The trend at a depth of 100 nm (not shown here) is similar. See more detail on the *piezospectroscopic* model that is described at the end of this paper in Section 4.1.

the side of the patch the number of components becomes four as observed in experiments.

We observe that, using the full *piezospectroscopic* model, at the patch center there are three split lines whereas in the experiments only two are visible. We interpret this as a combination of line broadening (much larger than the splitting), limited spectral resolution in experiments, and, potentially, different intensities associated with the split lines.[42,49,50]

2.3.1. Polarization Degree of the Zero Phonon Lines

Polarization-dependent micro-photoluminescence spectra of G-centers are registered for unstrained and strained samples (**Figure 7**). For unstrained G-centers (not covered by SiN), the ZPL is un-polarized, reflecting an even distribution of the emitting dipoles along the [110] and [1-10], in-plane directions (not shown).[51] At the center of the membrane, the LE line shows a negligible degree of polarization, whereas, for the HE one, it depends on the applied strain: in sample B, for $L = 13.2$ μm is about 3%, for $L = 12.1$ μm is 8% and for $L = 8.5$μm is 50% (here we only report the case of $L = 12.1$μm). The polarization direction of the HE line is close to the [1-1-3] direction, that in our reference frame corresponds to +30 degrees (Figure 7a).

At the edge of the patch, in the leaning part, un-polarized to almost fully-polarized ZPLs (up to 70%) are found, with the latter conditions typically observed for the high-energy component δ of the quadruplet that is oriented along the in-plane [12-1] direction (about 115° in our reference frame). Owing to a partial overlap of the split lines and their broadening, in these latter cases (e.g. as in Figure 6), it is not easy to extract the exact value of the polarization degree and our estimate is a lower bound. Similar results are observed at the corners of the membrane where the δ line
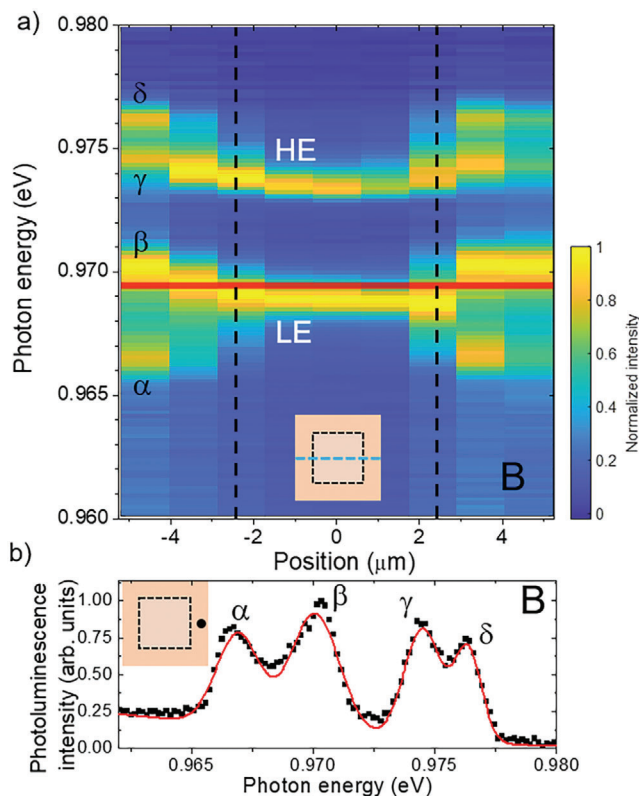

Figure 5. *Symmetry breaking along [001] and [110] direction.* a) Photoluminescence scan from patch side-to-side passing through the center (as highlighted in the inset). The vertical, dashed lines highlight the edge of the SiO2 pedestal. The horizontal, red line highlights the ZPL energy of unstrained G-centers. b) Photoluminescence spectrum at the side of the patch. The experimental data are shown as squares, whereas the red lines is a Gaussian fit. The insets show a scheme of the membrane and the position of the excitation/collection spot.
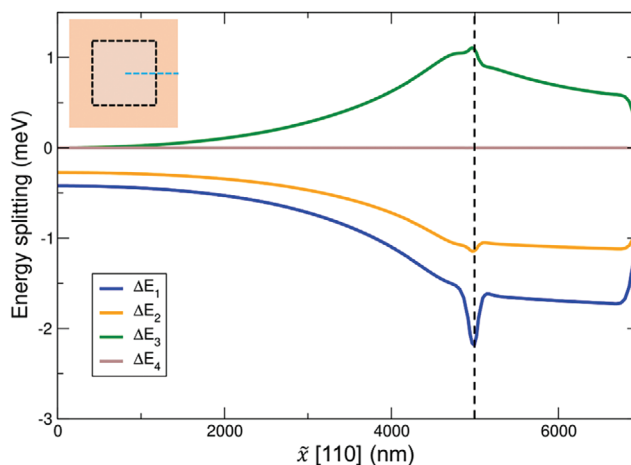

Figure 6. *Theoretical energy shift for symmetry breaking along [001] and [110] directions.* The plot showcases the shift of the four, split ZPLs as a function of position from the patch center to the edge as obtained from the *piezospectroscopic* model. We consider a patch having 14 μm side at a depth of 25 nm with $\epsilon_0 = 0.3\%$. The vertical, black, dashed line highlights the end of the SiO2 pedestal extending up to 5000 nm. The inset shows the scheme of the patch and the dashed, blue line highlights the position of the scan along the [110] direction considered in the model.
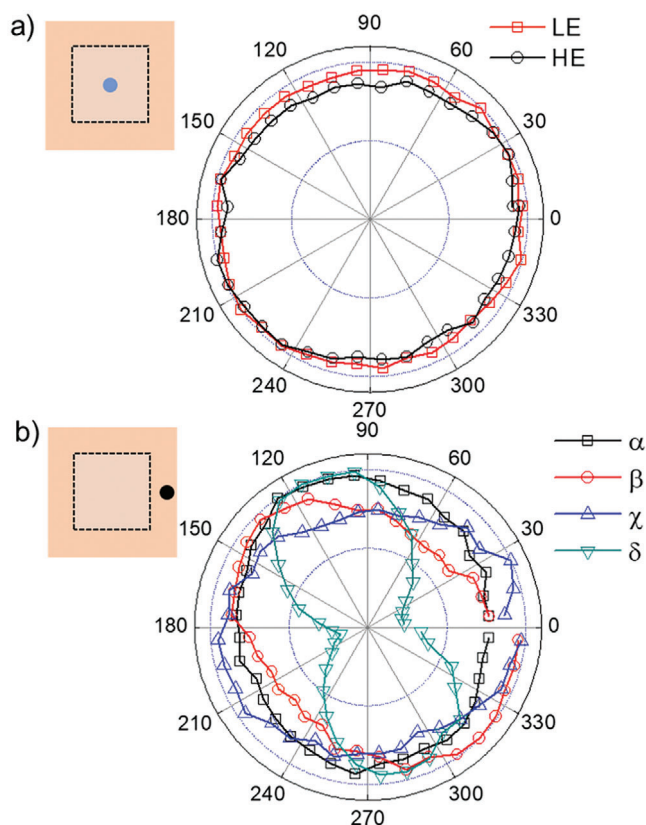
**ADVANCED
SCIENCE NEWS**

www.advancedsciencenews.com

**ADVANCED
OPTICAL
MATERIALS**

www.advopticalmat.de

Figure 7. *Polarization-resolved photoluminescence.* a) Polar plot of the HE and LE ZPLs from the central point of a membrane. b) Polar plot of the α, β, γ and δ ZPLs from the side of a patch. The insets show a scheme of the patch with the excitation/collection spot. All the data are relative to a patch with $L = 12.1$ μm on sample B.

has a polarization degree exceeding 50% (not shown). These observations qualitatively agree with previous reports of polarized photoluminescence on strained G-centers.[42,49,50]

2.4. Photoluminescence Enhancement

For sample B, we compare the emission intensity from the center of the patches with that from the flat SiN/SOI counterpart (**Figure 8**). We observe a clear trend showing an increased emission with a maximum enhancement of about a factor of 7 whereas, for larger values of L, the effect is reduced.

Provided the negligible impact of strain on the recombination lifetime that cannot justify the observed enhancement (Figure 3b) we look for a possible explanation in a photonic effect springing from the modified environment of the emitters in the membranes with respect to the flat SiN/SOI system. Through FDTD simulations (see a description of the simulation in Section 4.1) we compare the emission of a dipole placed at the center of the patch with respect to the same dipole in an infinite SiN/SOI (red circles in Figure 7). The trend of the simulated data corresponds well to the one observed in the experiments, supporting the idea that the origin of the enhancement resides in an augmented light extraction springing from the finite size of the patches.
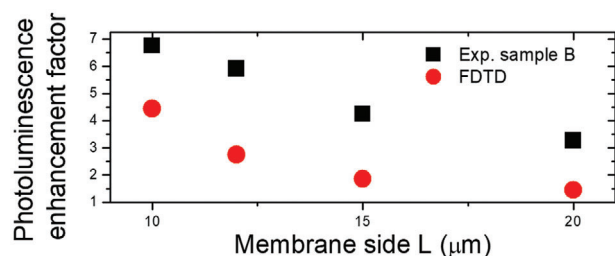

Figure 8. *Emission intensity.* Black squares: experimental emission enhancement from sample B. The data show the spectrally-integrated intensity of an individual spectrum collected at the center of the SiN/SOI membrane normalized by its counterpart from the flat areas (the collection spot is determined by the system lateral resolution and is about 1.1 μm). Red circles: FDTD simulations showing the spectrally integrated emission intensity normalized by its counterpart from the flat SOI.

Experiment and simulations display different enhancement factors (larger for experiments) that can be ascribed to the different conditions considered. Simulations consider only one dipole laying in the xy plane at a defined height whereas in rality we observe the emission from an ensemble of dipoles (excited by a laser spot and detected in a confocal configuration from about 1.1 μm), featuring several orientations and placed at slightly different depth in the SOI (Figure 2c).

3. Discussion

The phenomenology presented here is similar to what was shown in early studies on G-centers[48–50,52–54] and, more generally, to other color centers that belong to the symmetry group of the first monoclinic type C_{1h} in cubic crystals.[42,55] The photoluminescence splitting in a doublet that we find at the center of the patches mimics the effect of uniaxial strain along the [001] direction (no in-plane symmetry breaking). At the side of the patches, in the suspended part, where the Si cell symmetry is lifted also along the [110] direction, four split lines appear. These experimental findings qualitatively agree with predictions obtained through the *piezospectroscopic* model developed for strained cubic crystals.[42]

We showed this control with a very simple micro-structure, avoiding the use of bulky samples and experimental setups making use of hydraulic pistons to apply stress to the samples.[49,50] It is also worth pointing out that, beyond the present proof of principle that was limited to relatively large patches (L up to about 8 μm), the reduction of L to about 1 μm with conventional etching methods, or even below this value (e.g. exploiting solid state dewetting[22,56]), is possible. This could lead, potentially, to a stress that is more than one order of magnitude larger than what we show here, achieving strain regimes and polarization degrees not attained so far.

The importance of our results in the renewed context of quantum technologies with light-emitters in silicon is two-fold: 1) the possibility to control the splitting in a large range of energies (equivalent to a stress up to about 0.6 GPa[49,50]), allowing to tune the emission and, 2) the possibility to obtain, even from the ensemble, photoluminescence lines with a very large degree of linear polarization (as also reported in previous studies[42,49,50]), demonstrating that an ensemble of emitters shares the same energy and the same dipole orientation.

**ADVANCED
SCIENCE NEWS**

www.advancedsciencenews.com

**ADVANCED
OPTICAL
MATERIALS**

www.advopticalmat.de

The straggling of the ion implant might play a detrimental role for exploiting these emitters as quantum devices. On one hand, symmetry breaking along the [001] direction at the center of the membrane entails a uniform strain landscape in each of the three spatial directions. As such, whatever its position along z, an emitter will undergo the same splitting, shift, and polarization orientation as all the others. On the other end, for strain along the [110] direction (far from the center), the stress strongly depends on the position along the vertical z-axis: emitters created at different depth would undergo a different energy shift and splitting. Thus, in view of obtaining identical emitters (e.g. for quantum communication protocols), a reduction of struggling might be a hard requirement. This observation is also important for coupling the emitters to a localized photonic resonance.[31] Similar considerations hold for the high-temperature annealing step (required for re-crystallization after implant), which might spread the emitters over long distances along the vertical z-axis. However, in our case, where 1000 °C annealing for only 20 seconds was used, we do not expect a relevant re-distribution of carbon. In fact, even for strong changes of the strain profile along the SOI thickness (e.g. at the patch sides), for low-energy implants at about 25 nm depth, where the straggling is rather limited and all the emitters are within the first 50 nm from the surface, the photoluminescence showcases rather sharp ZPLs: the measured line-widths in sample B at the edge of the patch is 1-2 meV, not far from 0.9 meV found in the flat, non-strained counterpart. These observations indirectly confirm that for low-energy implant annealing at 1000 °C for 20 seconds does not affect too much the position of the implanted C ions in the SOI, unlike what was recently suggested based on theoretical simulations.[31]

A potential element of concern for strained emitters could be the change in the underlying oscillator strength, impacting their brightness. Although a complete understanding of these features is beyond the aim of this work, we note that, from time-resolved photoluminescence experiments, the lifetime is weakly affected by the strain. Moreover, when monitoring the overall emission intensity, we observe larger intensity values from the patches with respect to the flat areas. For smaller patches, this enhancement is almost one order of magnitude and it might be even larger for smaller ones.

This observation is important in the context of photoluminescence-intensity correlation with individual emitters (e.g. with Hanbury Brown and Twiss or Hong-Ou-Mandel interferometers), where light extraction is crucial for shortening the integration time of a measurement.

Very sharp linewidth from ensemble emission have been reported for impurities created in bulk ^{28}Si[14] accounting for the relevance of this platform for quantum optics, where high coherence is necessary (e.g. for photon coalescence). However, when using thin films of ^{28}Si on insulator to embed the emitters[17,20] this important feature disappears and linewidth in the range of ~100 μeV are found even when considering individual impurities. In addition to this, the statistical distribution of the ZPL emission of individual centers shows a broadening of about 1 meV (not far from the values found in the ensemble in conventional SOI). These observations point to additional extrinsic disorder in thin Si films affecting the overall recombination dynamics. Our study of SOI membranes embedding an ensemble of G-centers suggests that, beyond the intrinsic broadening of in-dividual emitters, an additional effect impacting the linewidth of the ZPL is the strain that can, in principle, change in different parts of the SOI (e.g. owing to slight fabrication imperfection or introduced by ion implant and re-crystallization). Further theoretical and experimental investigations are necessary to precisely address this important aspect of quantum emitters in silicon.

In spite of its simplicity and lack of Purcell effect, our method which uses only low-resolution optical lithography, allows for a relevant increase in the collection efficiency. Recent experimental evidences showed the possibility to largely enhance the emission intensity from G-centers enesemble embedded in Si-based Mie resonators.[22] In spite of the lack of Purcell effect in those measurements, contrary to what might be expected from a theoretical standpoint,[57] a directional emission is highly desirable to increase the collection efficiency with conventional optics. Our approach to tailor the electronic states can be, in principle, extended to such a kind of sub-micrometric antennas. Considering the scaling of the applied strain with $1/L^2$ and the small footprint of these antennas, a relatively thin SiN layer could be applied to Mie resonators resulting in a very large ZPLs splitting and polarization orientation.

The merit of our approach that relies on SOI lithography and deposition of a stressor film, is its compatibility with other devices, such as waveguides[30,31,36,37] and Mie resonators,[22,34,35] that are relevant to all the other quantum emitters in Si.[17,19–21,29,30] Our method can be generalized using suspended bridges providing uni-axial and bi-axial strain in arbitrary, in-plane directions.[58–62] Similar results can be obtained by deposition of stressors[63] or by deposition of Si atop a strained substrate (e.g. made of SiGe)[64] opening the way to finely control the position of the ZPL of the emitters (e.g. with respect to a photonic resonance of a resonant cavity). For instance, this possibility is central for tuning several independent sources to the same energy in order to produce coalescent photons, as shown for III-V-based quantum-emitters.[65] In the same context, the evidence of an almost fully-polarized line measured on the ensemble is a promising signature for aligning all the emitting dipoles along the same axis. For unstrained G-centers in fact, the dipole orientation can be aligned along the crystallographic directions [110], [101], and [011], depending on the position of the self-interstitial Si atom[51] providing unpolarized light from ensemble emission. Our method suggests the possibility to engineer the polarization axes, providing at least one split ZPL with the same orientation for all the emitters.

Finally, the possibility to control the degeneracy of the electronic level in G-centers, and more generally in this class of impurities in silicon, might be relevant for the manipulation of their spin features. Symmetry breaking by application of strain could be the way to split the metastable triplet state of the G-center[66,67] and thus encode spin-based quantum bits.[68–71] The fast recombination time of G-centers with respect to similar emitters in Si (e.g. the T-center[32–34]) would provide a more efficient read-out of the spin degree of freedom providing a spin-photon interface.

4. Conclusions

In conclusion, we showed that the splitting of the zero-phonon-line of the G-centers ensemble can be controlled producing doublets and quadruplets having large splittings, up to 18 meV, that

**ADVANCED
SCIENCE NEWS**

www.advancedsciencenews.com

**ADVANCED
OPTICAL
MATERIALS**

www.advopticalmat.de

is more than one order of magnitude larger than the broadening of the photoluminescence peaks. The splitting amplitude can be controlled by selecting a specific patch size. Symmetry breaking along [001] and [110] can be obtained respectively a the center of square patches and in their suspended parts. The merit of our approach is its simplicity, as it relies on conventional SiN deposition and lithography. It can be further engineered by changing patch geometry and orientation with respect to the crystallographic axes, SiN thickness and, most importantly, it can be easily extended to most common photonic devices. It will be possible to apply the same principle to other color centers in Si and access the fine features of the underlying recombination dynamics allowing to exploit of the spin degree of freedom for quantum technologies.

5. Experimental Section

Fabrication of Light-emitting, Strained Membranes: The sample fabrication is described in Figure 1 and the corresponding features are detailed in Table 1.

The samples are obtained by dicing a 125 nm thick SOI laying atop a 2 µm thick buried oxide (BOX) on bulk Si (from Soitec) in 1 cm × 1 cm parts. They were first implanted with carbon ions at a depth of 25 nm (samples A and B) and 100 nm (sample C) following a well-established procedure.[18,72] After the implant, all the samples were flash-annealed in N_2 atmosphere for 20 s at 1000° C to cure the radiation damages.

Each sample was patterned by optical lithography following this process:

- Chemical cleaning in a sonic bath, first with acetone and then with ethanol;
- Spin-coating of positive photo-resist (MICROPOSIT S1813) at 3000 rpm forming a layer of about 1.5 µm;
- Photo-lithography via UV laser system (Dilase 250 by Cloe). The pattern used for photoluminescence spectroscopy of strained G-centers consists of square patches whose size is tuned from about 15 to 5 µm;
- Resist development (using a solution from MICROPOSIT MF-319) to remove the parts that were not exposed to the UV laser;
- Pattern etching with a CF_4 plasma in a plasma-enhanced chemical vapor deposition chamber (PE-CVD, from Oxford);
- Sample cleaning with acetone;
- Partial etching of the BOX by immersion in an aqueous solution containing 10% of Buffered Oxide Etch (BOE 10:1) to form partially-suspended membranes;
- Deposition of a ~100nm thick SiN layer via PE-CVD. Three depositions are performed using different parameters changing the nature of the strain (tensile or compressive) applied to the SOI patches (Table 1). This is done by tuning the time percentage of high- and low-frequency plasma (HF%, which represents the fraction of time in which the high-frequency pulse is turned on with respect to the total pulse time expressed as a percentage). Changing HF% results in a compressive (HF < 60%), tensile (HF > 65%) or almost unstrained (60% < HF < 65%) SiN.[73] Ellipsometry (ESM-300 by Wollam) was systematically used to measure the thickness of the SiN layers deposited atop the SOI. The strained SiN affects the SOI patches resulting in a bent membrane, upwards for tensile strain, or downwards for compressive strain (Figure 1c));
- Implant with protons, to form the G-centers by inducing the interstitial Si.[74] The beam energy was set to 90 keV in order to stop the protons within the BOX, avoiding the activation of unwanted emitters in the SOI or in the underlying bulk Si.

Raman Spectroscopy Setup: Micro-Raman spectroscopy is performed at room temperature and is used to assess the stress in the flat samples and in the SOI patches. The setup consists of an Horiba-Jobin Yvon HR800-UV Raman spectrometer mounting a 1800 gpmm grating. It is characterized by a spectral resolution of about 0.5 cm^{-1}. The dispersed signal is then collected with a Jobin Yvon Synapse Si-based CCD camera. The samples are placed on a platform equipped with a $x - y$ translation stage to scan the sample surface and characterized by a spatial precision of about 250 nm. The samples are excited by a He:Ne laser ($\lambda = 632.8$ nm) through a 50× objective lens (Olympus SLMPLN50X) with a numerical aperture NA =0.35 mounted on a metallographic microscope (from Olympus). The Raman signal from the sample is collected via the same objective in a back-scattering configuration.

Micro-photoluminescence Spectroscopy Setup: The micro-photoluminescence spectra are detected with a custom-made confocal microscope setup in a backscattering configuration. The samples are placed in a low-vibration, He-flow cryostat (Janis ST-500), mounted on a $x - y$ translation stage (Physik Instruments) to scan the sample surface with fine control on the position of about 250 nm. The samples' temperature is fixed at about 10 K.

The excitation sources are a CW diode-pumped solid-state laser emitting at 532 nm (CNI MLL-III-532) and a mode-locked Ti:Sapphire tunable laser (Spectra Physics Tsunami, 700-900 nm spectral range, 200 fs pulse duration, 12.2 ns pulse period).

The photoluminescence from the samples is collected by an infinity-corrected Mitutoyo 100× objective lens (NIR, NA = 0.7), separated from the excitation by a dichroic mirror, spectrally dispersed by a spectrograph (Acton SP2300i) mounting a 600 gr/mm grating. The photoluminescence is detected by an InGaAs array (Princeton Instruments OMA V-512) kept at −100°~C by a cold finger immersed in liquid nitrogen.

The spatial resolution of the micro-photoluminescence setup is about 1.1 µm, and the spectral resolution is about 350 µeV.

Time-resolved PL (TR-PL) measurements were performed using the time-correlated single photon counting (TCSPC) technique using an InGaAs/InP APD (ID Quantique ID230) and a time correlator (ID Quantique ID900) interfaced with the PC. The time resolution of the system is about 200 ps.

Polarization measurements are performed by placing a rotatable half-wave plate and a fixed polarizer along the collection path.

Finite Element Method Simulations of Strain Distribution: The strain distribution in the system is computed by 3D Finite Element Method (FEM) calculations based on the linear elasticity theory[60,75] exploiting the commercial FEM package COMSOL Multiphysics. To model the experimental structure under investigation, we consider a square bilayer formed by a SiN layer of 100 nm atop a 125 nm thick silicon layer. This layer is supported at the center by a SiO_2 pillar with a square base. The whole structure is placed on a silicon substrate. The suspended part of the SiN/Si bilayer, from its edge to the edge of the SiO_2 pedestal, is 2 µm (independently of the lateral extension of the membrane). Simulations are performed for structures with a center-to-edge extension of the SiN on SOI ranging between 6 and 16 µm whereas the bottom SiO_2 (see Figure 2a), mimicking the geometry shown in Figure 1b and c)).

The elastic field is then computed by the FEM simulations to satisfy the mechanical equilibrium condition (without external forces), $\nabla \cdot \boldsymbol{\sigma} = 0$, the free surface boundary condition, $\boldsymbol{\sigma} \cdot \hat{\mathbf{n}} = 0$ with $\hat{\mathbf{n}}$ the normal to the free surface(s), and the Dirichlet boundary condition $\mathbf{u} = 0$ with $\mathbf{u}$ the displacement field for the silicon substrate similarly to previous investigations of mechanical stress in heteroepitaxial systems.[46,76]

The stress field is defined as $\boldsymbol{\sigma} = \mathbf{C} : (\boldsymbol{\varepsilon} - \epsilon_0 \mathbf{I})$ with $\boldsymbol{\varepsilon} = (1/2)(\nabla \mathbf{u} + (\nabla \mathbf{u})^T)$ the strain field and ϵ_0 the eigenstrain,[77] namely minus the mismatch of the SiN layer with respect to the Si layer induced by the growth process. ϵ_0 is found to vary according to the fabrication condition in the range ±1%. The elastic constant tensor $\mathbf{C}$ is assumed to be isotropic for the purposes of this work. Expressed in terms of Young modulus (E) and Poisson ratio (ν) they are: E_{Si}=130 GPa, ν_{Si}=0.27, E_{SiN}=250 GPa, ν_{SiN}=0.23, E_{SiO_2}=70 GPa, ν_{SiO_2}=0.17.

We explicitly consider only the case of a SiN layer under compressive strain. However, the resulting strain distributions scale linearly with ϵ_0. Therefore, as we are interested in the ratios between different strain components, their distributions are provided in relative units w.r.t such an eigenstrain.

**ADVANCED
SCIENCE NEWS**

www.advancedsciencenews.com

**ADVANCED
OPTICAL
MATERIALS**

www.advopticalmat.de

Theoretical piezospectroscopic Model: The behavior of non-cubic color centers in cubic crystals can be described by adopting a *piezospectroscopic* method[42,50,78] coupling the observed energy splitting of the center spectral lines with the strain field. The transition energy shift in the emission of a center, ΔE, can be written as:

$$\Delta E = \sum_{k,l} B_{kl} \epsilon_{kl} \tag{1}$$

where ϵ_{kl} are the strain field components (with kl pointing at the canonical frame of reference), and B_{kl} some coefficients which form a second rank symmetric tensor.[42] Both experimental[48,49,67] and first principles studies[51,67,79] have clearly demonstrated that G-centers, which consist of two substitutional carbons and one interstitial silicon atom, behave as first-type monoclinic centers (C_{1h}) with an axis along the [110] direction. In this case, the number of coefficients B_{kl} is reduced to four, and Equation 1 can be rewritten as:

$$\Delta E = B_1 \epsilon_{zz} + B_2 (\epsilon_{xx} + \epsilon_{yy}) + 2B_3 \epsilon_{xy} + 2B_4 (\epsilon_{yz} - \epsilon_{xz}) \tag{2}$$

Depending on the particular strain field, Equation 2 can be further simplified. More specifically, in the case of a tensile or compressive deformation along the [100] direction, the number of split spectral lines is two, whereas it corresponds to four when the deformation is along the [110] direction. In the first case, Equation 2 becomes:

$$\Delta E = B_1 \epsilon_{zz} + B_2 (\epsilon_{xx} + \epsilon_{yy}) \tag{3}$$

Assuming that the energy separation ΔE is composed by an high energy shift, ΔE_{HE}, and a low energy shift, ΔE_{LE} (corresponding to the two split spectral lines) Equation 4 can be written as:

$$\Delta E_{HE} + \Delta E_{LE} = B_1 \epsilon_{zz} + B_2 (\epsilon_{xx} + \epsilon_{yy}) \tag{4}$$

if this equality holds, then:

$$\Delta E_{HE} = E_{HE} - E_0 = B_1 \epsilon_{zz}$$
$$\Delta E_{LE} = E_{LE} - E_0 = B_2 (\epsilon_{xx} + \epsilon_{yy}) \tag{5}$$

where E_0 is the ZPL (0.969 eV). Eqs. 5 can be finally written as:

$$E_{HE} = B_1 \epsilon_{zz} + E_0$$
$$E_{LE} = B_2 (\epsilon_{xx} + \epsilon_{yy}) + E_0 \tag{6}$$

On the other hand, when the deformation is along the [110] direction, the non-diagonal components of the strain tensor cannot be neglected. In this case, the number of split lines is four, and Equation 2 has to be fully taken into account.

We employed both versions of Equation 2 (full and simplified one) to theoretically evaluate the shift of the G-center ZPL moving from the center to the side of the patches. The strain field, ϵ_{kl}, is computed by 3D FEM calculations as described above while B_{kl} coefficients are taken from previous works on [100] and [110] strained cubic Si.[48] However, in our study, Equation 2 assumes a slightly more complex form. Indeed, as is shown in Figure 2, the strain field ϵ_{kl} is a function of the distance from the center of the patch, d. As a consequence, Equation 2 becomes:

$$\Delta E(d) = B_1 \epsilon_{zz}(d) + B_2 [\epsilon_{xx}(d) + \epsilon_{yy}(d)] + 2B_3 \epsilon_{xy}(d) + 2B_4 [\epsilon_{yz}(d) - \epsilon_{xz}(d)] \tag{7}$$

and, in the same way, Eqs. 6 can be written as:

$$E_{HE}(d) = B_1 \epsilon_{zz}(d) + E_0$$
$$E_{LE}(d) = B_2 [\epsilon_{xx}(d) + \epsilon_{yy}(d)] + E_0 \tag{8}$$

In this way, we build a predictive model to prove that the measured ZPL energy shifts are due to the difference in the strain field between the center and the side of the patches. Moreover, such a model can also demonstrate that the dependence of ΔE on $1/L^2$ (where L is the patch side) is linear.

Finite Difference Time Domain Simulations of Light Emission: Calculations of light emission from the etched patches were performed by Finite Difference Time Domain (FDTD) method employing the commercial software Lumerical. To simulate the emission from a single G-center, an x-polarized, spectrally narrow, light-emitting electric dipole is used, centered around 0.970 eV with a pulse length of 3000 fs. We simulate two kinds of systems: 1) an infinite multilayer structure composed by (from top to bottom) a 100 nm thick SiN layer, a 125 nm thick SOI layer, and a 2 μm thick SiO$_2$ layer atop a Si bulk. 2) Square patches of different sides are modeled analogously to the one used in FEM simulations described before, except made for the strain effect which is not included in these FDTD simulation domain. In both cases (infinite multilayer and finite size membranes) the dipole is positioned at 25 nm from the upper surface of the SOI layer (at the center of the membrane for the finite patch cases). A 2D monitor geometrically configured to reproduce an acquisition of NA = 0.7, is positioned atop of the multilayered structures and collects the signal coming from the system. The intensity is then calculated by integrating the emission over the monitor area (12 μm × 12 μm). For the sake of thoroughness, we also studied different configurations by changing the monitor distance from the multilayer and adjusting the monitor size in order to reproduce the experimental NA of 0.7. No significant differences were highlighted, and this analysis is not reported.

Supporting Information

Supporting Information is available from the Wiley Online Library or from the author.

Conflict of Interest

The authors declare no conflict of interest.

Data Availability Statement

The data that support the findings of this study are available from the corresponding author upon reasonable request.

**ADVANCED
SCIENCE NEWS**

www.advancedsciencenews.com

**ADVANCED
OPTICAL
MATERIALS**

www.advopticalmat.de

[1] V. Sverdlov, *Strain-induced effects in advanced MOSFETs*, Springer Science & Business media, Berlin/Heidelberg **2011**.

[2] S. E. Thompson, G. Sun, Y. S. Choi, T. Nishida, *IEEE Trans. Electron Devices* **2006**, *53*, 1010.

[3] J. Welser, J. L. Hoyt, J. F. Gibbons, *IEEE Electron Device Lett.* **1994**, *15*, 100.

[4] C. Si, Z. Sun, F. Liu, *Nanoscale* **2016**, *8*, 3207.

[5] Z. Dai, L. Liu, Z. Zhang, *Adv. Mater.* **2019**, *31*, 1805417.

[6] J. Ben, X. Liu, C. Wang, Y. Zhang, Z. Shi, Y. Jia, S. Zhang, H. Zhang, W. Yu, D. Li, X. Sun, *Adv. Mater.* **2021**, *33*, 2006761.

[7] Large-scale and high-quality III-nitride membranes through microcavity-assisted crack propagation by engineering tensile-stressed Ni layers. **2022**.

[8] T. Liu, H. Li, T. He, C. Fan, Z. Yan, D. Liu, Q. Sun, Ultra-high resolution strain sensor network assisted with an LS-SVM based hysteresis model. **2021**.

[9] *Materials Science and Engineering: R: Reports* **2010**, *70*, 320. 3rd IEEE International NanoElectronics Conference (INEC).

[10] J. A. Del Alamo, *Nature* **2011**, *479*, 317.

[11] M. Amato, M. Palummo, R. Rurali, S. Ossicini, *Chem. Rev.* **2014**, *114*, 1371.

[12] *Materials Science in Semiconductor Processing* **2017**, *70*, 117.

[13] G. Davies, S. Hayama, L. Murin, R. Krause-Rehberg, V. Bondarenko, A. Sengupta, C. Davia, A. Karpenko, *Phys. Rev. B* **2006**, *73*, 165202.

[14] C. Chartrand, L. Bergeron, K. J. Morse, H. Riemann, N. V. Abrosimov, P. Becker, H.-J. Pohl, S. Simmons, M. L. W. Thewalt, *Phys. Rev. B* **2018**, *98*, 195201.

[15] M. Khoury, M. Abbarchi, *J. Appl. Phys.* **2022**, *131*, 200901.

[16] A. Lohrmann, B. C. Johnson, J. C. McCallum, S. Castelletto, *Rep. Prog. Phys.* **2017**, *80*, 034502.

[17] Y. Baron, A. Durand, P. Udvarhelyi, T. Herzig, M. Khoury, S. Pezzagna, J. Meijer, I. Robert-Philip, M. Abbarchi, J.-M. Hartmann, V. Mazzocchi, J.-M. Gérard, A. Gali, V. Jacques, G. Cassabois, J.-M. Dréau, *ACS Photonics* **2022**, *9*, 2337.

[18] C. Beaufils, W. Redjem, E. Rousseau, V. Jacques, A. Y. Kuznetsov, C. Raynaud, C. Voisin, A. Benali, T. Herzig, S. Pezzagna, J. Meijer, M. Abbarchi, G. Cassabois, *Phys. Rev. B* **2018**, *97*, 035303.

[19] A. Durand, Y. Baron, W. Redjem, T. Herzig, A. Benali, S. Pezzagna, J. Meijer, A. Y. Kuznetsov, J.-M. Gérard, I. Robert-Philip, M. Abbarchi, V. Jacques, G. Cassabois, A. Dréau, *Phys. Rev. Lett.* **2021**, *126*, 083602.

[20] Y. Baron, A. Durand, T. Herzig, M. Khoury, S. Pezzagna, J. Meijer, I. Robert-Philip, M. Abbarchi, J.-M. Hartmann, S. Reboh, J.-M. Gérard, V. Jacques, G. Cassabois, A. Dréau, *Appl. Phys. Lett.* **2022**, *121*, 084003.

[21] W. Redjem, A. Durand, T. Herzig, A. Benali, S. Pezzagna, J. Meijer, A. Y. Kuznetsov, H. S. Nguyen, S. Cueff, J.-M. Gérard, I. Robert-Philip, B. Gil, D. Caliste, P. Pochet, M. Abbarchi, V. Jacques, A. Dréau, G. Cassabois, *Nat. Electron.* **2020**, *3*, 738.

[22] M. Khoury, H. Quard, T. Herzig, J. Meijer, S. Pezzagna, S. Cueff, M. Abbarchi, H. S. Nguyen, N. Chauvin, T. Wood, *Adv. Opt. Mater.* **2022**, *10*, 2201295.

[23] C. C. Lo, A. Persaud, S. Dhuey, D. Olynick, F. Borondics, M. C. Martin, H. A. Bechtel, J. Bokor, T. Schenkel, *Semicond. Sci. Technol.* **2009**, *24*, 105022.

[24] K. M. Itoh, H. Watanabe, *MRS Commun.* **2014**, *4*, 143.

[25] P. Becker, D. Schiel, H. J. Pohl, A. K. Kaliteevski, O. N. Godisov, M. F. Churbanov, G. G. Devyatykh, A. V. Gusev, A. D. Bulanov, S. A. Adamchik, V. A. Gavva, I. D. Kovalev, N. V. Abrosimov, B. Hallmann-Seiffert, H. Riemann, S. Valkiers, P. Taylor, P. De Biévre, E. M. Dianov, *Meas. Sci. Technol.* **2006**, *17*, 1854.

[26] R. Maurand, X. Jehl, D. Kotekar-Patil, A. Corna, H. Bohuslavskyi, R. Laviéville, L. Hutin, S. Barraud, M. Vinet, M. Sanquer, S. De Franceschi, *Nat. Commun.* **2016**, *7*, 1.

[27] V. Mazzocchi, P. G. Sennikov, A. D. Bulanov, M. F. Churbanov, B. Bertrand, L. Hutin, J. P. Barnes, M. N. Drozdov, J. M. Hartmann, M. Sanquer, *J. Cryst. Growth* **2019**, *509*, 1.

[28] D. Sabbagh, N. Thomas, J. Torres, R. Pillarisetty, P. Amin, H. C. George, K. Singh, A. Budrevich, M. Robinson, D. Merrill, L. Ross, J. Roberts, L. Lampert, L. Massa, S. V. Amitonov, J. M. Boter, G. Droulers, H. G. J. Eenink, M. van Hezel, D. Donelson, M. Veldhorst, L. M. K. Vandersypen, J. S. Clarke, G. Scappucci, *Phys. Rev. Appl.* **2019**, *12*, 014013.

[29] M. Hollenbach, Y. Berencén, U. Kentsch, M. Helm, G. V. Astakhov, *Opt. Express* **2020**, *28*, 26111.

[30] M. Prabhu, C. Errando-Herranz, L. De Santis, I. Christen, C. Chen, D. R. Englund, *arXiv preprint arXiv:2202.02342* **2022**.

[31] L. Komza, P. Samutpraphoot, M. Odeh, Y.-L. Tang, M. Mathew, J. Chang, H. Song, M.-K. Kim, Y. Xiong, G. Hautier, A. Sipahigil, *arXiv preprint arXiv:2211.09305* **2022**.

[32] L. Bergeron, C. Chartrand, A. T. K. Kurkjian, K. J. Morse, H. Riemann, N. V. Abrosimov, P. Becker, H.-J. Pohl, M. L. W. Thewalt, S. Simmons, *Phys. Rev. X. Quantum* **2020**, *1*, 020301.

[33] L. Bergeron, C. Chartrand, A. Kurkjian, A. T. K. Kurkjian, K. J. Morse, H. Riemann, N. V. Abrosimov, P. Becker, H.-J. Pohl, M. L. W. Thewalt, S. Simmons, *arXiv preprint arXiv:2006.08794* **2020**.

[34] D. B. Higginbottom, A. T. K. Kurkjian, C. Chartrand, M. Kazemi, N. A. Brunelle, E. R. MacQuarrie, J. R. Klein, N. R. Lee-Hone, J. Stacho, M. Ruether, C. Bowness, L. Bergeron, A. DeAbreu, S. R. Harrigan, J. Kanaganayagam, D. W. Marsden, T. S. Richards, L. A. Stott, S. Roorda, K. J. Morse, M. L. W. Thewalt, S. Simmons, *Nature* **2022**, *607*, 266.

[35] M. Hollenbach, N. S. Jagtap, C. Fowley, J. Baratech, V. Guardia-Arce, U. Kentsch, A. Eichler-Volf, N. V. Abrosimov, A. Erbe, C. Shin, H. Kim, M. Helm, W. Lee, G. V. Astakhov, Y. Berencén, *J. Appl. Phys.* **2022**, *132*, 033101.

[36] A. DeAbreu, C. Bowness, A. Alizadeh, C. Chartrand, N. A. Brunelle, E. R. MacQuarrie, N. R. Lee-Hone, M. Ruether, M. Kazemi, A. T. K. Kurkjian, S. Roorda, N. V. Abrosimov, H.-J. Pohl, M. L. W. Thewalt, D. B. Higginbottom, S. Simmons, *arXiv preprint arXiv:2209.14260* **2022**.

[37] B. Lefaucher, J. B. Jager, V. Calvo, A. Durand, Y. Baron, F. Cache, V. Jacques, I. Robert-Philip, G. Cassabois, T. Herzig, J. Meijer, S. Pezzagna, M. Khoury, M. Abbarchi, A. Dréau, J.-M. Gérard, *Appl. Phys. Lett.* **2023**, *122*.

[38] C. E. Herranz, C. Gerlach, L. De Santis, C. Panuski, M. Prabhu, H. Raniwala, I. Christen, D. Englund, *Bull. Am. Phys. Soc.* **2022**.

[39] W. Redjem, Y. Zhiyenbayev, W. Qarony, V. Ivanov, C. Papapanos, W. Liu, K. Jhuria, Z. A. Balushi, S. Dhuey, A. Schwartzberg, L. Tan, T. Schenkel, B. Kanté, All-silicon quantum light source by embedding an atomic emissive center in a nanophotonic cavity, **2023**, https://arxiv.org/abs/2301.06654.

[40] M. Hollenbach, N. Klingner, N. S. Jagtap, L. Bischoff, C. Fowley, U. Kentsch, G. Hlawacek, A. Erbe, N. V. Abrosimov, M. Helm, Y. Berencén, G. V. Astakhov, *Nat. Commun.* **2022**, *13*, 1.

[41] D. B. Higginbottom, F. K. Asadi, C. Chartrand, J.-W. Ji, L. Bergeron, M. L. W. Thewalt, C. Simon, S. Simmons, *PRX Quantum* **2023**, *4*, 020308.

[42] A. A. Kaplyanskii, *Le Journal de Physique Colloques* **1967**, *28*, C4.

[43] J. F. Ziegler, M. D. Ziegler, J. P. Biersack, *Nuclear Instruments and Methods in Physics Research Section B: Beam Interactions with Materials and Atoms* **2010**, *268*, 1818.

[44] J. E. Ayers, T. Kujofsa, P. Rago, J. Raphael, *Heteroepitaxy of semiconductors: theory, growth, and characterization*, CRC press, Boca Raton, FL **2016**.

[45] F. Glas, *Phys. Rev. B* **2006**, *74*, 121302.

[46] M. Salvalaglio, F. Montalenti, *J. Appl. Phys.* **2014**, *116*, 104306.

[47] L. B. Freund, J. A. Floro, E. Chason, *Appl. Phys. Lett.* **1999**, *74*, 1987.

[48] V. D. Tkachev, A. V. Mudryi, *J. Appl. Spectrosc.* **1978**, *29*, 1485.

[49] C. P. Foy, M. C. do Carmo, G. Davies, E. C. Lightowlers, *Journal of Physics C: Solid State Physics* **1981**, *14*, L7.

[50] K. Thonke, H. Klemisch, J. Weber, R. Sauer, *Phys. Rev. B* **1981**, *24*, 5874.

[51] P. Udvarhelyi, B. Somogyi, G. Thiering, A. Gali, *Phys. Rev. Lett.* **2021**, *127*, 196402.

[52] A. V. Yukhnevich, *Sov. Phys. Solid State* **1965**, *7*, 322.

[53] A. V. Yukhnevich, *Fiz. Tverd. Tela* **1965**, *7*.

[54] A. V. Yuknevich, A. V. Mudryi, *Fiz. Tekh. Poluprovdn* **1973**, [Sov. Phys. Semicond. 7, 815 (1973) 7 1215.

[55] G. Baumann, F. Lanzl, W. Von Der Osten, W. Waidelich, *Le Journal de Physique Colloques* **1967**, *28*, C4.

[56] D. Toliopoulos, M. Khoury, M. Bouabdellaoui, N. Granchi, J.-B. Claude, A. Benali, I. Berbezier, D. Hannani, A. Ronda, J. Wenger, M. Bollani, M. Gurioli, S. Sanguinetti, F. Intonti, M. Abbarchi, *Opt. Express* **2020**, *28*, 37734.

[57] Q. Deng, J. Chen, L. Long, B. Chen, H. Yu, Z. Li, *Opto-Electronic Advances* **2022**, *5*, 210024.

[58] F. Ureña, S. H. Olsen, J.-P. Raskin, *J. Appl. Phys.* **2013**, *114*, 144507.

[59] M. J. Süess, R. Geiger, R. A. Minamisawa, G. Schiefler, J. Frigerio, D. Chrastina, G. Isella, R. Spolenak, J. Faist, H. Sigg, *Nat. Photonics* **2013**, *7*, 466.

[60] M. Bollani, D. Chrastina, L. Gagliano, L. Rossetto, D. Scopece, M. Barget, V. Mondiali, J. Frigerio, M. Lodari, F. Pezzoli, F. Montalenti, E. Bonera, *Appl. Phys. Lett.* **2015**, *107*, 083101.

[61] M. R. Barget, M. Lodari, M. Borriello, V. Mondiali, D. Chrastina, M. Bollani, E. Bonera, *Appl. Phys. Lett.* **2016**, *109*, 133109.

[62] A. Gassenq, S. Tardif, K. Guilloy, I. Duchemin, N. Pauc, J. M. Hartmann, D. Rouchon, J. Widiez, Y. M. Niquet, L. Milord, T. Zabel, H. Sigg, J. Faist, A. Chelnokov, F. Rieutord, V. Reboud, V. Calvo, *J. Appl. Phys.* **2017**, *121*, 055702.

[63] D. Scopece, F. Montalenti, M. Bollani, D. Chrastina, E. Bonera, *Semicond. Sci. Technol.* **2014**, *29*, 095012.

[64] T. David, I. Berbezier, J.-N. Aqua, M. Abbarchi, A. Ronda, N. Pons, F. Domart, P. Costaganna, G. Uren, L. Favre, *ACS Appl. Mater. Interfaces* **2020**, *13*, 1807.

[65] J. Q. Grim, A. S. Bracker, M. Zalalutdinov, S. G. Carter, A. C. Kozen, M. Kim, C. S. Kim, J. T. Mlack, M. Yakes, B. Lee, D. Gammon, *Nat. Mater.* **2019**, *18*, 963.

[66] K. O'donnell, K. M. Lee, G. D. Watkins, *Physica B+ C* **1983**, *116*, 258.

[67] V. Ivanov, J. Simoni, Y. Lee, W. Liu, K. Jhuria, W. Redjem, Y. Zhiyenbayev, C. Papapanos, W. Qarony, B. Kanté, A. Persaud, T. Schenkel, L. Z. Tan, *Phys. Rev. B* **2022**, *106*, 134107.

[68] S. Arroyo-Camejo, A. Lazariev, S. W. Hell, G. Balasubramanian, *Nat. Commun.* **2014**, *5*, 1.

[69] C. Zu, W.-B. Wang, L. He, W.-G. Zhang, C.-Y. Dai, F. Wang, L.-M. Duan, *Nature* **2014**, *514*, 72.

[70] S. Foletti, H. Bluhm, D. Mahalu, V. Umansky, A. Yacoby, *Nat. Phys.* **2009**, *5*, 903.

[71] X. Wu, D. R. Ward, J. R. Prance, D. Kim, J. K. Gamble, R. T. Mohr, Z. Shi, D. E. Savage, M. G. Lagally, M. Friesen, S. N. Coppersmith, M. A. Eriksson, *Proc. Natl. Acad. Sci.* **2014**, *111*, 11938.

[72] D. D. Berhanuddin, M. A. Lourenço, R. M. Gwilliam, K. P. Homewood, *Adv. Funct. Mater.* **2012**, *22*, 2709.

[73] F. Karouta, K. Vora, J. Tian, C. Jagadish, *J. Phys. D: Appl. Phys.* **2012**, *45*, 445301.

[74] D. D. Berhanuddin, M. A. Lourenço, R. M. Gwilliam, K. P. Homewood, *Adv. Funct. Mater.* **2012**, *22*, 2709.

[75] L. D. Landau, E. M. Lifšic, E. M. Lifshitz, A. M. Kosevich, L. P. Pitaevskii, *Theory of elasticity: volume 7*, vol. 7, Elsevier, Amsterdam **1986**.

[76] R. Bergamaschini, M. Salvalaglio, R. Backofen, A. Voigt, F. Montalenti, *Adv. Phys.: X* **2016**, *1*, 331.

[77] N. Kinoshita, T. Mura, *Phys. Status Solidi A* **1971**, *5*, 759.

[78] A. Hughes, *Proc. Phys. Soc.* **1966**, *87*, 535.

[79] D. Timerkaeva, C. Attaccalite, G. Brenet, D. Caliste, P. Pochet, *J. Appl. Phys.* **2018**, *123*, 161421.